for submission to The Astrophysical Journal.
Preprint typeset using LaTeX style emulateapj v. 10/09/06



# A MEASUREMENT OF THE ANGULAR POWER SPECTRUM OF THE CMB TEMPERATURE ANISOTROPY FROM THE 2003 FLIGHT OF BOOMERANG

W. C. Jones[1], P. A. R. Ade[2], J. J. Bock[3], J. R. Bond[4], J. Borrill[5,6], A. Boscaleri[7], P. Cabella[8], C. R. Contaldi[4,9], B. P. Crill[10], P. de Bernardis[11], G. De Gasperis[8], A. de Oliveira-Costa[12], G. De Troia[11], G. Di Stefano[13], E. Hivon[10], A. H. Jaffe[9], T. S. Kisner[14,15], A. E. Lange[1], C. J. MacTavish[16], S. Masi[11], P. D. Mauskopf[2], A. Melchiorri[11,17], T. E. Montroy[15], P. Natoli[8,18], C. B. Netterfield[16,19], E. Pascale[16], F. Piacentini[11], D. Pogosyan[4,20], G. Polenta[11], S. Prunet[21], S. Ricciardi[11], G. Romeo[13], J. E. Ruhl[15], P. Santini[11], M. Tegmark[12], M. Veneziani[11], N. Vittorio[8,18]

*for submission to The Astrophysical Journal.*

## ABSTRACT

We report on observations of the Cosmic Microwave Background (CMB) obtained during the January 2003 flight of BOOMERANG. These results are derived from 195 hours of observation with four 145 GHz Polarization Sensitive Bolometer (PSB) pairs, identical in design to the four 143 GHz *Planck* HFI polarized pixels. The data include 75 hours of observations distributed over 1.84% of the sky with an additional 120 hours concentrated on the central portion of the field, itself representing 0.22% of the full sky. From these data we derive an estimate of the angular power spectrum of temperature fluctuations of the CMB in 24 bands over the multipole range $50 \leq \ell \leq 1500$. A series of features, consistent with those expected from acoustic oscillations in the primordial photon-baryon fluid, are clearly evident in the power spectrum, as is the exponential damping of power on scales smaller than the photon mean free path at the epoch of last scattering ($\ell \gtrsim 900$). As a consistency check, the collaboration has performed two fully independent analyses of the time ordered data, which are found to be in excellent agreement.

*Subject headings:* Cosmic Microwave Background, Cosmology, Bolometers

## 1. INTRODUCTION

The wealth of cosmological information that is encoded in the statistical properties of the Cosmic Microwave Background Radiation (CMB) has motivated a highly successful observational effort to measure the angular power spectrum of the CMB temperature anisotropies. The experimental effort is broad based, with teams reporting results from interferometric and single dish observations spanning a decade in frequency and more than three decades in angular scale [for some recent results, see Bennett et al. (2003a); Benoît et al. (2003); Ruhl et al. (2003); Halverson et al. (2002); Readhead et al. (2004); Kuo et al. (2004); Dickinson et al. (2004); Lee et al. (2001)]. The success of these observations, coupled with the predictive power of accurate theoretical modeling, has contributed to the ongoing transformation of cosmology into a quantitative, precise, and increasingly accurate science.

In this paper, we present the angular power spectrum of the temperature anisotropies derived from the data obtained during the January 2003 flight of BOOMERANG (hereafter B03). Having been upgraded with a polarization sensitive receiver [Montroy et al. (2003); Masi et al. (2005)], B03 is optimized to probe the polarization of the CMB at sub-degree angular scales while retaining full sensitivity to the unpolarized emission. In addition to a measurement of the curl-free component of the CMB polarization [Montroy et al. (2005)] and the temperature-polarization cross correlation [Piacentini et al. (2005)], the 2003 flight has resulted in a precise measurement of the angular power spectrum of the temperature anisotropies.

These data represent an improvement on published measurements of the temperature power spectrum at multipoles $600 \lesssim \ell \lesssim 1200$, which probe physical scales corresponding to the photon mean free path during the epoch of last scattering.

## 2. INSTRUMENT AND OBSERVATIONS

Following the successful 1998 Antarctic campaign [de Bernardis et al. (2000); Netterfield et al.

[1] Physics Department, California Institute of Technology, Pasadena, CA, USA (wcj@astro.caltech.edu)
[2] School of Physics and Astronomy, Cardiff University, UK
[3] Jet Propulsion Laboratory, Pasadena, CA, USA
[4] Canadian Institute for Theoretical Astrophysics (CITA), University of Toronto, ON, Canada
[5] Computational Research Division, LBNL, Berkeley, CA, USA
[6] Space Sciences Laboratory, University of California at Berkeley, CA, USA
[7] IFAC-CNR, Firenze, Italy
[8] Dipartimento di Fisica, Università di Roma "Tor Vergata", Rome, Italy
[9] Theoretical Physics Group, Imperial College, London, UK
[10] Infrared Processing and Analysis Center, California Institute of Technology, Pasadena, CA, USA
[11] Dipartimento di Fisica, Università di Roma "La Sapienza", Rome, Italy
[12] Department of Physics, Massachusetts Institute of Technology, Cambridge, MA, USA
[13] Instituto Nazionale di Geofisica e Vulcanologia, Rome, Italy
[14] Department of Physics, University of California at Santa Barbara, CA, USA
[15] Department of Physics, Case Western Reserve University, Cleveland, OH, USA
[16] Department of Physics, University of Toronto, ON, Canada
[17] INFN, Sezione di Roma 1, Rome, Italy
[18] INFN, Sezione di Roma 2, Rome, Italy
[19] Department of Astronomy and Astrophysics, University of Toronto, ON, Canada
[20] Department of Physics, University of Alberta, Edmonton, AB, Canada
[21] Institut d'Astrophysique de Paris, Paris, France

(2002); Ruhl et al. (2003); Crill et al. (2003)], an entirely new focal plane was designed around a set of four 145 GHz Polarization Sensitive Bolometer (PSB) pairs. These receivers, the first of their kind to be used in astronomical observations, combine the raw sensitivity of cryogenic bolometers with intrinsic sensitivity to linear polarization, a property historically associated only with coherent detectors [Jones (2005); Jones et al. (2003); Montroy (2002)].

In addition to the four 145 GHz PSB pixels, the B03 focal plane accommodates four dual-frequency photometers, operating in bands centered near 245 and 345 GHz. While the CMB temperature anisotropies are detected with high signal to noise in the 245 and 345 GHz data [Montroy (2002); Masi et al. (2005)], these data are not included in the present analysis.

### 2.1. *Polarization Sensitive Bolometers*

Each bolometer within a PSB pair is sensitive to a linear combination of the Stokes $I$, $Q$, and $U$ parameters on the sky multiplied by the frequency response of the receiver, $F_\nu$, and convolved with the (two-dimensional) co- and cross-polar beam patterns, $P_\parallel(\hat{r})$ and $P_\perp(\hat{r})$, respectively. After deconvolving the system transfer function from the time ordered data, each sample from a single detector within a PSB pair, $d_i$, may be written as the sum of a signal component

$$\begin{array}{l} d_i = \frac{s}{2}\int d\nu \frac{\lambda^2}{\Omega_b} F_\nu \int\int d\hat{r}\ (P_\parallel(\hat{r}_i) + P_\perp(\hat{r}_i)) \\ \left[\ I + \gamma\ \mathcal{P}(\hat{r}_i)\ \left(Q\cos 2\psi_i + U \sin 2\psi_i\ \right)\right], \end{array} \tag{1}$$

and a noise contribution. The Stokes parameters are understood to be defined on the full sky, and the integration variable is $\hat{r}_i = \hat{n}_i - \hat{r}$, for a vector, $\hat{n}_i$, describing the pointing at a time sample, $i$. The normalized beam response and the polarization efficiency are given by,

$$\mathcal{P}(\hat{r}) \equiv \frac{P_\parallel - P_\perp}{P_\parallel + P_\perp} \qquad \gamma \equiv \frac{1-\epsilon}{1+\epsilon}\ . \tag{2}$$

The polarization leakage parameter, $\epsilon$, is defined as the ratio of the square of the diagonal elements of the Jones matrix describing an imperfect polarizer. For B03's PSBs, the leakage ranges from 5% to 8%, as determined from pre-flight measurements. The angle $\psi$ is the projection of the axis of sensitivity of a given detector on the sky. This angle is modulated in time due to sky rotation, and is further affected by the motion of the gondola. The calibration factor, $s$, that converts the brightness fluctuations in $I$, $Q$, and $U$ to a signal voltage, is obtained through cross-calibration with the temperature anisotropies observed by WMAP [Bennett et al. (2003b); Masi et al. (2005)].

A more detailed discussion of the PSB design may be found in Jones et al. (2003). A description of the characterization of the B03 PSBs may be found in Masi et al. (2005). A discussion regarding properties and methods of analysis of PSBs may be found in Jones et al. (2005) and Jones (2005).

### 2.2. *Sky Coverage*

The BOOMERANG gondola scans in azimuth, mapping the sky signal to a bandwidth between ∼50 mHz and 5 Hz. Sky rotation modulates the orientation of the instrument with respect to the signal. A complete characterization of the Stokes $I$, $Q$ and $U$ parameters is achieved via a combination of this sky rotation as well as the joint analysis of the data from all eight detectors in the course of pixelization. The low frequency stability of the bolometric system and balloon environment allow an accurate reconstruction of all three linear Stokes parameters at each pixel with sensitivity to angular scales ranging from $\sim 10^\circ$ to the $\sim 10'$ beamsize.

TABLE 1
B03 INSTRUMENT SUMMARY

| $\langle\nu\rangle$ GHz | MJy/sr / $K_{CMB}$ | $\theta_{phys}$ FWHM | $\theta_{eff}$ [a] FWHM | NET [b] $\mu K_{CMB}\sqrt{s}$ | $\sigma_{pix}$ [c] $\mu K_{CMB}$ |
|---|---|---|---|---|---|
| 145 | 388 | $9.95'$ | $11.5'$ | 63 | 18 |
| 245 | 462 | $6.22'$ | $8.5'$ | 161 | 50 |
| 345 | 322 | $6.90'$ | $9.1'$ | 233 | 72 |

[a] The effective beam is defined as the convolution of the physical beam with the $\simeq 2.4'$ *r.m.s.* error in the pointing reconstruction as determined from point source observations in the CMB field.[b] The focal plane noise equivalent temperature, derived from the in-flight noise measured at 1 Hz. Note, however, that at both low (< 100 mHz) and high (> 5 Hz) frequencies, the noise rises significantly.[c] The approximate noise ($\approx \langle \mathrm{diag}(\mathbf{C}_N)\rangle$) per $3.4'$ pixel in the deep field for the data included in this analysis.

The launch date, latitude, and the azimuth/elevation constraints imposed by solar, limb, and balloon avoidance considerations limit the region of sky accessible to BOOMERANG. During the Austral summer, the anti-solar meridian falls in the vicinity of RA $\simeq 70^\circ$ (J2000 epoch). Continuum emission from the Galaxy is significant over much of the available sky; the CMB field is chosen to minimize this Galactic contamination, subject to the constraints imposed by the LDB flight parameters.

The BOOMERANG telescope is an Alt-Az mount that is scanned in azimuth at constant elevation. The elevation is adjusted on hour time scales. The pendulation frequencies of the gondola and scan rate limitations constrain the minimum peak to peak scan amplitude to approximately 15°. Earth's rotation provides about 20° of cross linking between scans, which aides in the decorrelation of the Stokes parameters. When the local hour angle (modulo twelve hours) is in the vicinity of the RA of the target field (*i.e.*, when the sky rotation, and therefore the cross-linking, is minimal), our scans are redirected to the Galactic plane.

Given B03's instantaneous sensitivity, the amplitude of the CMB polarization signal motivates us to concentrate as much integration time as possible in as small a region as possible. However, the competing desire to make high fidelity measurements of (the relatively large amplitude) unpolarized temperature fluctuations led us to a two-tiered scan strategy, representing a compromise between sensitivity to the temperature and polarization power spectra.

During the first four days of the flight, seventy-five hours were dedicated to observations covering $\simeq 1.84\%$ of the sky (these observations are referred to as the "shallow field"), while an additional 175 hours of observation were concentrated on the central portion of this field

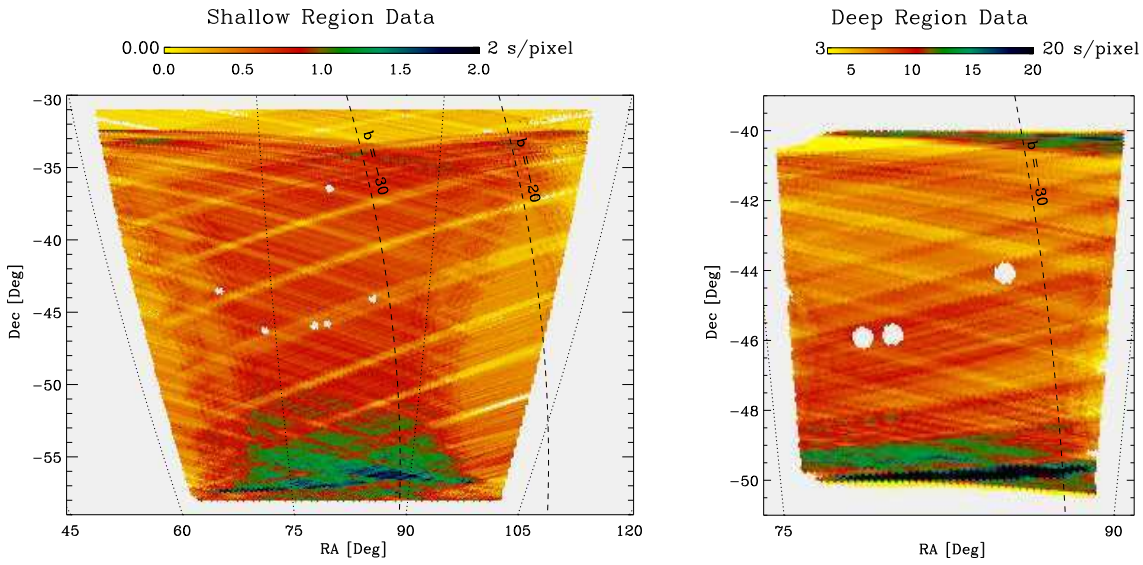


FIG. 1.— The left and right panels show the sky coverage obtained during the January 2003 flight of BOOMERANG. The integration times per $3.4'$ pixel are shown for the shallow and deep data subsets described in the text. Galactic latitude contours of $b = \{-30, -20\}$ are shown for reference. Approximately 75 hours of observation are devoted to the shallow region, with an additional 120 hours concentrated in the central deep field. The cross-linking of the scans due to sky rotation is evident in the diagonal striping of the coverage, which has a $\approx 20^\circ$ opening angle. Known extragalactic point sources, shown masked in these plots, are excluded from the analysis.

(the "deep region"). The deep field constitutes roughly $\simeq 0.22\%$ of the full sky. The exact distributions of integration time for the data included in this analysis are shown in Figure 1. The B03 sky coverage is a subset of the region observed during BOOMERANG's 1998 flight.

### 2.3. *Inflight Calibration*

Both the calibration of the receivers and the characterization of the effective beam must be obtained from the inflight data. The former is due to the dependence of the bolometer responsivity on the radiative background, while the latter depends on the fidelity of the pointing reconstruction.

The calibrations are obtained from the CMB itself; both the CMB dipole and degree-scale anisotropies provide a well calibrated signal with precisely the desired spectrum. Scan synchronous noise limits the accuracy of the dipole calibration to $\sim 15\%$. As described in Masi et al. (2005), cross-correlation with the WMAP data [Bennett et al. (2003a)] provides an absolute calibration uncertainty of 1.8%, including the uncertainty in the WMAP calibration. The B03 calibration is limited by the relatively low signal-to-noise of the WMAP data at degree angular scales. The relative calibrations of the B03 detectors are obtained from cross-correlations of single channel temperature maps, and are accurate to 0.8%.

The error in the inflight pointing reconstruction is estimated from the angular size of the extragalactic point sources in the B03 CMB fields. As indicated in Table 1, the effective beams are consistent with the physical optics model of the optical system, convolved with a $2.4'$ *r.m.s.* Gaussian pointing jitter. Measurements of five bright sources in the shallow and deep fields provide an estimated $0.23'$ FWHM uncertainty on the width of the effective beams.

## 3. ANALYSIS

As a probe of the robustness of both the data and its analysis, the BOOMERANG team has implemented two fully independent analyses of the B03 time ordered data. The two pipelines, one centered in North America (NA) and one in Italy (IT), are described in detail in Masi et al. (2005), Contaldi et al. (2005), Jones et al. (2005), de Gasperis et al. (2005) and references therein. In this section, we summarize the general approach to signal, noise, and angular power spectrum estimation.

### 3.1. *Signal/Noise Estimation*

Estimates of the signal on the sky and noise in the timestreams are obtained using an iterative procedure similar to that applied to the B98 temperature data [Netterfield et al. (2002); Prunet et al. (2001); Ruhl et al. (2003)]. Least squares maps of the Stokes I, Q, and U parameters are generated from a combined analysis of the data from all eight 145 GHz PSBs, corresponding to roughly $3 \cdot 10^8$ time domain samples. The data from each channel are weighted by their NET and combined during pixelization to decorrelate the linear Stokes parameters at each pixel. The Stokes parameter maps are generated at $\simeq 3.4'$ resolution, resulting in approximately 377000 spatial pixels.

The NA team divides the timestream into 200 noise-stationary subsets. The noise power spectra are calculated from each of these chunks using the converged estimate of the signal derived from the full set of data. Each of these spectra are corrected for bias using an ensemble of signal and noise Monte Carlos. The IT analysis assumes stationarity of the noise over the course of the flight. While the NA approach is more general, the IT analysis benefits from a reduction in the sample variance of the noise estimate in the time domain. Each team employs a self-consistent treatment of the correlated noise

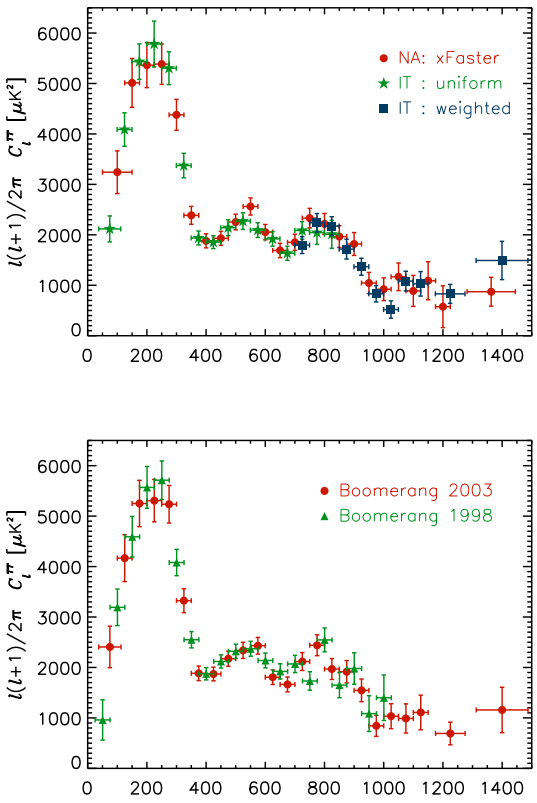


FIG. 2.— In the top panel, we show a comparison of the temperature angular power spectrum derived from the B03 data using the NA pipeline (xFaster, in red circles) and the IT pipeline, the latter using both uniform (green stars) and noise weighted (blue squares) masks. For the IT results, uniform weighting of the combined shallow and deep data results in nearly optimal errorbars in the signal-dominated regime, while the $1/\sqrt{N_{obs}}$ pixel weighting is required to achieve this sensitivity in the noise dominated regime. The NA spectrum is derived using a hybrid auto- and cross- correlation technique which achieves nearly optimal errors across the full multipole range. In the lower panel, a comparison of the angular power spectrum derived from the B98 data [Ruhl et al. (2003)], and the B03 results reported here. The 2003 coverage is a sub-set of the region observed in 1998, so the signal is completely correlated between the two datasets. The binning of the B03 data in the lower panel is shifted by half of a bin relative to the top panel.

between channels. Details regarding the two signal and noise estimation pipelines are provided in Jones et al. (2005), and de Gasperis et al. (2005).

### 3.2. *Power Spectrum Estimation*

Both the NA and IT analysis pipelines employ variations of the pseudo-$C_\ell$ Monte Carlo approach to power spectrum estimation introduced in Hivon et al. (2002). Each incorporates a polarized implementation of a general least squares signal estimator. The IT team uses a traditional pseudo-$C_\ell$ approach using either $1/\sqrt{N_{obs}}$ *or* uniformly weighted masks to derive the temperature power spectrum, while a cross-correlation technique similar to that described in Tristram et al. (2005) and Polenta et al. (2004) is used for the polarization analysis. Unlike these approaches, the NA estimator of the temperature and polarization power spectra is based on a hybrid auto- and cross-correlation technique adapted for multiple data sets characterized by partially overlapping sky coverage [Contaldi et al. (2005)].

As described in Hivon et al. (2002), the Monte Carlo approach approximates the spherical harmonic transform of the *heuristically weighted* data, $\widetilde{C}_\ell^{TT}$, as a convolution over the underlying power spectrum, $C_{\ell'}^{TT}$, with an additive noise term, $\widetilde{N}_\ell$.

$$\widetilde{C}_\ell^{TT} = \sum_{\ell'} K_{\ell\ell'} B_{\ell'}^2 F_{\ell'} C_{\ell'}^{TT} + \widetilde{N}_\ell \qquad (3)$$

The coupling kernel, $K_{\ell\ell'}$, is derived analytically from the transform of the weighted mask that has been applied to the data. The window function, $B_\ell$, is the transform of the effective beam on the sky, and approximates the convolution over the Stokes parameters appearing in Equation 1. The transfer function, $F_\ell$, is a symmetrized approximation of the combined effect of the scan strategy and time-domain processing on the sensitivity to a given angular scale.

The transfer function is determined from an ensemble of signal-only Monte Carlo simulations, while the noise pseudo-power spectrum, $\widetilde{N}_\ell$, is obtained from an ensemble of noise-only simulations. Both the signal and noise simulations treat the flagged portions of the time stream in exactly the same manner as the actual data.

### 3.3. *The B03 Temperature Power Spectrum*

The Monte Carlo approach to power spectrum estimation represents an approximate treatment of the noise covariance matrix of the map, and therefore generally results in larger uncertainties than do direct methods [Borrill (1999)]. The sensitivity achieved by a Monte Carlo estimate of the power spectrum is determined by the properties of the noise and the weighting applied to the data.

When analyzing a single map generated from the full set of B03 data, a complication arises in the selection of the weighting that is applied to the mask. In the limit of white (that is, pixel-uncorrelated) noise, the optimal power spectrum estimate of a noise-dominated signal is obtained by weighting the pixels according to $1/\sqrt{N_{obs}}$. For the combined set of shallow and deep data, this scheme is therefore virtually equivalent to analyzing *only* the deep region. Conversely, in the signal dominated regime a uniform weighting will reduce (to the extent possible) the sample variance in the band power estimates. The choice of weighting reflects a trade-off between the optimality of errorbars at low and high multipoles. For the B03 data, the angular power spectrum is signal dominated at multipoles below $\ell \lesssim 900$, as indicated in the fourth column of Table 2.

The IT temperature power spectrum is derived from an analysis of the combined shallow and deep field data, using an approach similar to that applied to the B98 data in Netterfield et al. (2002) and Ruhl et al. (2003). The IT analysis is carried out using *either* uniform *or* $1/\sqrt{N_{obs}}$ pixel weighting. The agreement between the NA and IT analyses, as well as with the B98 results reported in Ruhl et al. (2003), is illustrated in Figure 2. These results, representing two independent datasets and no less

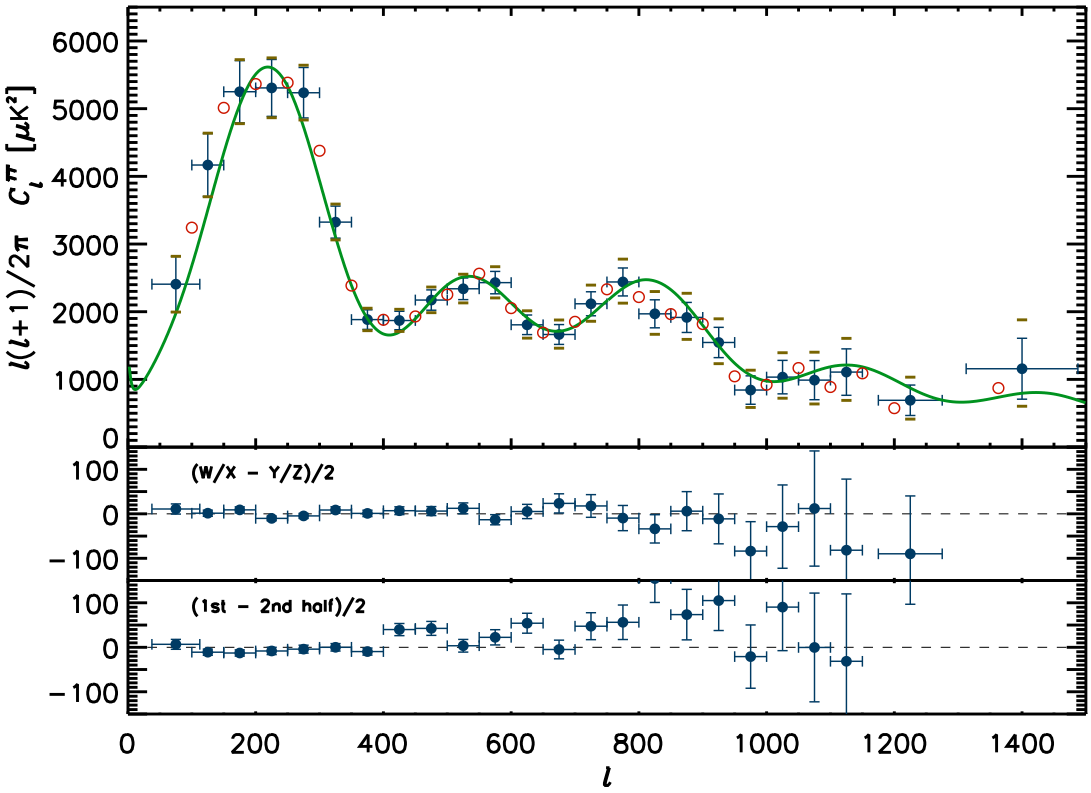


FIG. 3.— The temperature angular power spectrum, $\mathcal{C}_\ell^{\rm TT}$, derived from the B03 data. The red points represent an alternate binning, and should not be interpreted as having statistical weight beyond that of the nominally binned data, which are shown with errorbars. The anti-correlations between neighboring bands range from the twelve to twenty percent level. The envelope of the beam uncertainty is indicated by ticks bracketing the one sigma errorbars for each of the bandpower estimates. As discussed in Section 3.5, these limits indicate the amount of "tilt" to the spectrum that is allowed by the beam uncertainty, and should not be interpreted as an additional uncorrelated error in each bin. The solid green line is the concordance ΛCDM model which best fits all published CMB data, including the B03 temperature and polarization results. The power spectra of the consistency checks described in the text are shown in the lower two panels.

than three independent analysis pipelines, are indicative of the robustness of the result.

The NA pipeline addresses the problem of heuristic weighting of data with uneven coverage by treating the shallow and deep time ordered data separately. Each of these subsets, which have roughly uniform noise per pixel, exhibit partially correlated signal and statistically independent noise. A uniform weighting is applied to the shallow data, while the deep data are noise weighted.

Estimates of the underlying power spectra are derived from the joint analysis of the two auto-spectra *and* the cross-power spectrum of the shallow and deep data, using a diagonal approximation to the quadratic Fisher matrix estimator. The inclusion of both the auto and cross power spectra allows nearly optimal errors to be obtained over the full range of angular scales, while computing the complete Fisher matrix in a self-consistent fashion for all the bandpowers (temperature and polarization) simultaneously [Contaldi et al. (2005)].

The full resolution B03 spectrum is displayed with the best fit concordance ΛCDM model in the upper panel of Figure 3 [MacTavish et al. (2005)]. The maximum likelihood bandpowers, the diagonal components of the correlation matrix, and the ratio of sample to noise variance are presented in Table 2. As indicated in the fourth column of this table, the spectrum is sample variance limited at multipoles below $\ell \lesssim 900$. Neighboring bins are anti-correlated at the $\simeq$ 12–20% level, the variation resulting from the exact form of the masks and the multipole binning.

The B03 data improve on the published measurements of the temperature angular power spectrum primarily over the third peak, at angular scales corresponding to the photon mean free path at the surface of last scattering. All of the B03 temperature and polarization power spectra, inverse Fisher matrices, window functions and explanatory supplements are publicly available on the BOOMERANG web servers[1].

### 3.4. *Internal Consistency Tests*

As a check on the internal consistency of the data, we perform two complete jackknife tests in which the TOD are divided in two halves, and $I$, $Q$, and $U$ maps are generated from each half independently. The power spectra are then computed from the difference of the resultant maps.

The temporal jackknife divides the data into a first half and a second half, in which the shallow and deep scans are each divided in order to ensure roughly equal cover-

[1] `http://cmb.phys.cwru.edu/boomerang/index.html`
`http://oberon.roma1.infn.it/boomerang/b2k`

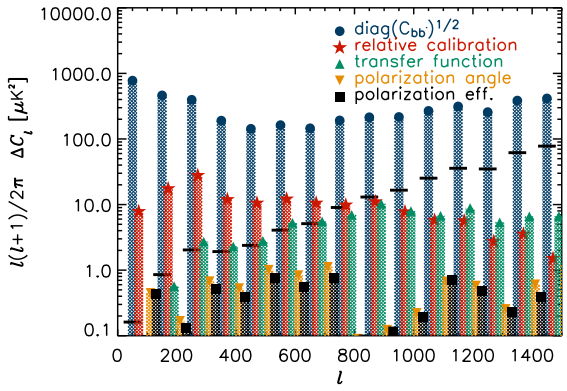


FIG. 4.— The propagation of instrumental calibration errors to the bandpower estimates. The amplitude of the statistical uncertainties (sample variance plus instrumental noise) for each bin are shown with circles. The contributions from the relative calibration, $s \pm 0.8\%$, the the in-flight transfer function $\tau \pm 10\%$, the polarization angle, $\psi \pm 2^\circ$, and polarization efficiency $\epsilon \pm 3\%$ are shown for reference. The horizontal ticks indicate the effect of beam uncertainty. Note that each of these effects are highly correlated between bins, and therefore are not properly treated by quadrature addition to the statistical uncertainty in a given bin. Since the correlation structure of these errors is known, they are more properly treated as nuisance parameters, and as such are marginalized over during the cosmological parameter estimation [Bridle et al. (2002)]. For the B03 parameter extraction, only the beam error and calibration uncertainty are treated in this manner [MacTavish et al. (2005)].

age of the sky in each subset. As discussed in Masi et al. (2005) and Jones (2005), B03 experienced a dramatic ($\simeq$ 9km) loss of altitude over the course of the flight. The first-half/second-half test was chosen to provide a check which is maximally sensitive to systematic effects related to the altitude drop, such as responsivity drifts, a degradation in the accuracy of the pointing reconstruction, or atmospheric contamination.

The channel jackknife measures the difference between maps generated from the two halves of the focal plane. Each side of the focal plane accommodates two pairs of PSBs, allowing complete characterization of the three linear Stokes parameters. The sky coverage, filtering, and data flagging of this jackknife test are nearly identical to that of the full data set.

The noise properties, and therefore the inverse noise filtering of the signal, varies slightly from channel to channel. When the data are processed in the time domain, this asymmetry, combined with the channel specific flagging of the time ordered data, results in a non-zero difference spectrum even in a noiseless observation free of systematic effects. The temporal jackknife is similarly affected; the observations are not symmetric for the two subsets of data, resulting in subtle differences in the signal processing. For both the channel-based and temporal divisions of the data, this offset is easily characterized in the Monte Carlo analysis by performing the same consistency test on an ensemble of simulations. The ensemble average of these simulated difference spectra are directly subtracted from those derived from the data.

The high signal to noise ratio with which the temperature anisotropies are detected is evident in the spectra of the differenced data, which are shown in the lower two panels of Figure 3. The first of these is the spectrum of the difference generated from the channel based division, the second is the spectrum derived from the temporal division. While the former (with a $\chi^2 = 20.8$ for 24 degrees of freedom) passes the jackknife test, the latter clearly fails ($\chi^2 = 55.5$). The failure of the first-half/second-half consistency test, though significant, is at an amplitude which is small compared to the uncertainty from instrumental noise and sample variance in all but the last two bins, as shown in Table 2.

TABLE 2
THE BOOMERANG 03
TEMPERATURE POWER SPECTRUM

| $\ell_b$ | $\mathcal{C}_b$ | $\Delta\mathcal{C}_b$ | $\mathcal{C}_b/\mathcal{N}_b$ | (WX-YZ)/2 | (1st-2nd)/2 |
|---|---|---|---|---|---|
| 75 | 2406 | 410 | 12.28 | 11 ± 11 | 7 ± 11 |
| 125 | 4167 | 464 | 28.25 | 1 ± 7 | -11 ± 7 |
| 175 | 5250 | 459 | 117.66 | 9 ± 7 | -13 ± 7 |
| 225 | 5306 | 420 | 132.13 | -10 ± 5 | -8 ± 8 |
| 275 | 5235 | 372 | 125.39 | -5 ± 6 | -4 ± 9 |
| 325 | 3323 | 236 | 72.60 | 9 ± 7 | 0 ± 8 |
| 375 | 1884 | 144 | 12.89 | 1 ± 7 | -10 ± 8 |
| 425 | 1870 | 136 | 7.71 | 7 ± 9 | 40 ± 14 |
| 475 | 2172 | 149 | 5.97 | 6 ± 10 | 42 ± 16 |
| 525 | 2338 | 159 | 4.45 | 12 ± 12 | 3 ± 14 |
| 575 | 2429 | 165 | 3.37 | -13 ± 11 | 22 ± 17 |
| 625 | 1806 | 144 | 1.97 | 5 ± 16 | 54 ± 22 |
| 675 | 1663 | 146 | 1.45 | 24 ± 22 | -5 ± 21 |
| 725 | 2117 | 177 | 1.41 | 18 ± 26 | 47 ± 30 |
| 775 | 2440 | 206 | 1.28 | -10 ± 28 | 56 ± 39 |
| 825 | 1968 | 207 | 0.90 | -34 ± 32 | 154 ± 54 |
| 875 | 1915 | 221 | 0.78 | 6 ± 44 | 73 ± 57 |
| 925 | 1545 | 223 | 0.61 | -11 ± 56 | 105 ± 67 |
| 975 | 842 | 209 | 0.37 | -84 ± 66 | -21 ± 71 |
| 1025 | 1034 | 247 | 0.38 | -29 ± 94 | 90 ± 98 |
| 1075 | 989 | 289 | 0.32 | 12 ± 129 | 0 ± 122 |
| 1125 | 1108 | 343 | 0.32 | -82 ± 160 | -31 ± 151 |
| 1225 | 691 | 224 | 0.13 | -90 ± 130 | 225 ± 128 |
| 1400 | 1157 | 449 | 0.06 | -611 ± 343 | 702 ± 301 |

The angular power spectrum of the B03 temperature data and the results of the consistency tests described in Section 3.4. The bandpowers, $C_b$ $\ell_b(\ell_b+1)/2\pi$ and their errors are in units of $[\mu\mathrm{K}^2]$. The full set of temperature and polarization angular power spectra, and the associated covariance matrices and window functions, are publicly available on the BOOMERANG web servers, `http://cmb.phys.cwru.edu/boomerang/index.html` and `http://oberon.roma1.infn.it/boomerang/b2k`. Neighboring bins are anticorrelated at the 12% to 20% level, depending on the multipole bin. The errors, $\Delta\mathcal{C}_b$, are taken from the diagonal elements of the covariance matrix. In particular, the diagonal elements of the covariance matrix can be approximated by the formula $\Delta C_b \simeq \sqrt{\frac{2}{(2\ell_b+1)\ \Delta\ell\ f_{sky}\ \mathcal{F}_b}}\,(C_b + N_b)$, where $\mathcal{F}_b \leq 1$ is a parameterization of the mode loss resulting from the filtering applied to the data. The $N_b$ term represents the (binned and deconvolved) power spectrum of the noise, as determined from noise only simulations. Therefore, the ratio $C_b/N_b$ indicates the relative contribution of sample and noise variance for a given bandpower. This quantity is shown for reference in the fourth column. The bandpowers obtained from the two consistency tests described in 3.4 are given in the last two columns. We have subtracted the ensemble averaged power spectra derived from the jackknifes of the signal and noise Monte Carlos. The $\chi^2$ to zero for the channel (temporal) jackknife is $\chi^2 = 20.8(55.5)$ for 24 degrees of freedom.

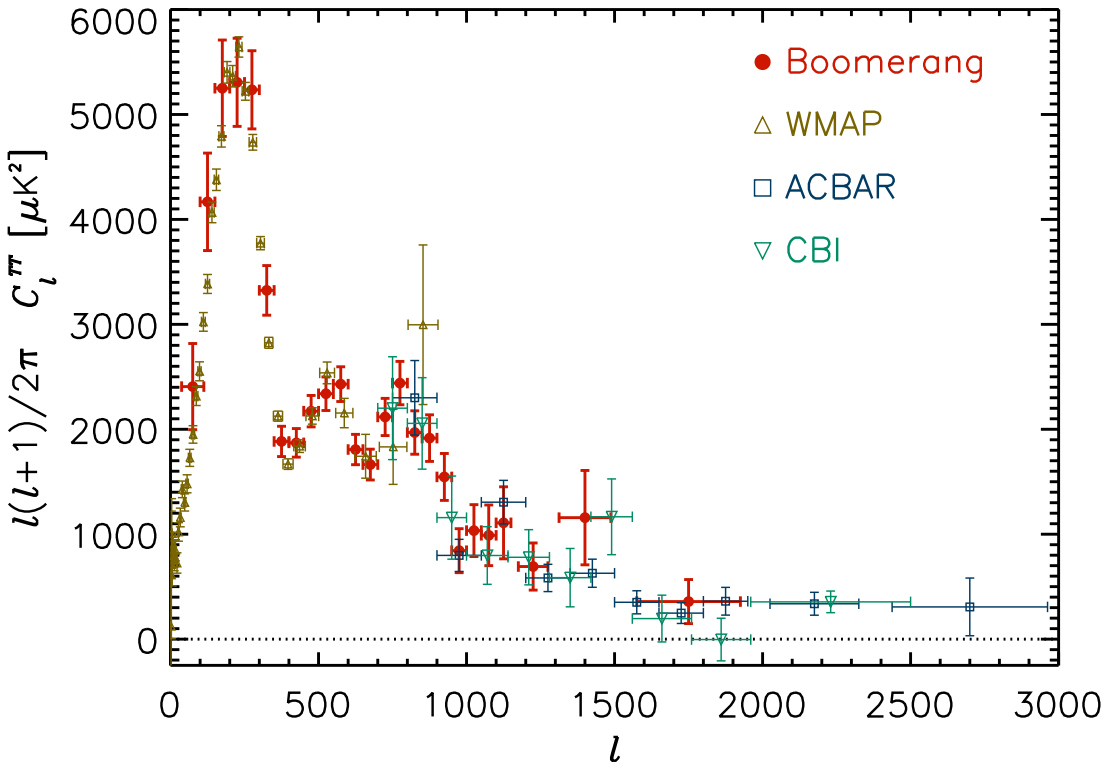


FIG. 5.— A comparison of recently published CMB power spectra, $\mathcal{C}_\ell^{\rm TT}$, [the data shown are from Hinshaw et al. (2003); Kuo et al. (2004); Readhead et al. (2004), in addition to B03]. The data shown are derived from independent measurements that span two orders of magnitude in electromagnetic frequency (20-200 GHz), employ both single dish and interferometric instruments, and operate from terrestrial, balloon-borne, and orbital platforms. The remarkable degree of accord between such a diverse set of measurements is indicative of the maturity of the observational field.

### 3.5. *Propagation of Systematic Errors*

Uncertainties in the calibration and low level analysis of the data propagate in a complicated way from the TOD to the band power estimates. For the B03 analysis the principle uncertainties are the determination of the inflight transfer functions, the relative calibrations, the polarization efficiencies, and the effective beamsize.

A very powerful feature of the Monte Carlo approach is the ease with which such effects can be modeled *as they appear in the time domain*, and properly accounted for in the analysis of the power spectra. In particular, we investigate the impact of the uncertainty in the polarization leakage ($\epsilon$, $\pm 3\%$), the PSB orientation in the focal plane ($\psi$, $\pm 2^\circ$), and the relative calibration ($s$, $\pm 0.8\%$) that appear in Equations 1 and 2. Additionally, we probe the impact of the uncertainty on the inflight system transfer function (parameterized by a single-pole time-constant $\tau$, $\pm 10\%$) that is used to deconvolve each of the bolometer timestreams at the earliest stage of the analysis[2].

A simulated TOD is generated for each B03 channel using a realization of the best fit concordance ΛCDM cosmology while randomly varying the instrumental parameters about their nominal values. An ensemble of these TODs are processed through the NA analysis pipeline, and the distribution of the resultant bandpowers are used to propagate uncertainties on the instrumental parameters to systematic errorbars on the band power estimates. The results of this analysis, shown in Figure 4, indicate that B03 is not limited by systematics resulting from uncertainties in the characterization of the instrument.

It is straightforward to analytically determine the impact of an uncertainty on the effective beamsize on the bandpower estimates. An estimate of the beam uncertainty is obtained from fits to the five brightest extragalactic sources in the CMB field. In the limit that the pointing errors are Gaussian and isotropic, this misestimation will lead to a bias in spectrum equal to the ratio of the estimated and underlying window functions. This bias has a known spectrum

$$W'_\ell / W_\ell = e^{-\sigma_b^2\ (\delta^2 + 2\delta)\ \ell(\ell+1)}\ , \qquad (4)$$

for an effective beam of width $\sigma_b = \theta_{\rm FWHM}/\sqrt{8\ln 2}$, and a fractional error, $\delta$. The envelope of the two-sigma limits corresponding to a beam uncertainty of $\delta \simeq \pm 2\%$ are shown as ticks bracketing the errorbars in Figure 3.

The effects of both instrumental calibration and beam uncertainty are highly correlated from bin to bin, and have a known spectrum (Equation 4), or are only weakly dependent on the underlying spectrum of the signal. As such, they are both properly treated as nuisance parameters rather than independent contributions to the uncertainty in each bin. In the B03 parameter estimation, the calibration and beam uncertainty are treated in this manner, following closely the prescription of Bridle et al. (2002).

[2] The bolometer transfer function is dependent on the inflight loading conditions and, for B03, is difficult to determine with the required accuracy from the inflight data itself. See Jones (2005) and Masi et al. (2005) for further discussion of this topic.

### 3.6. *Foreground Contamination*

Galactic microwave emission can potentially contaminate observations of the CMB. At 150 GHz, the thermal emission of interstellar dust grains is expected to be the dominant component of galactic emission [Brandt et al. (1994); de Oliveira-Costa (2004); Masi et al. (2001)]. Therefore any galactic contamination in the 143 GHz B03 data is expected to exhibit some spatial correlation with existing infrared surveys. The spectrum of the galactic continuum emission is distinct from that of the CMB, allowing multifrequency observations to discriminate between the cosmological signal and local foregrounds. For this reason, B03 made simultaneous observations at 245 and 345 GHz.

Using the method described in de Oliveira-Costa et al. (1999), we quantify the level of foreground contamination in the B03 145 GHz data by cross-correlating the Stokes I parameter map with the Schlegel-Finkbeiner-Davis (SFD) dust map. The SFD map is a composite of the all-sky DIRBE and IRAS 100$\mu$m surveys [Hauser et al. (1998); Neugebauer et al. (1984); Finkbeiner et al. (1999); Schlegel et al. (1998)].

We estimate the uncertainty on the correlation by applying the same analysis to fifty B03 noise realizations. Before calculating the correlations, we resample the DIRBE/IRAS data with the B03 scan pattern and filtering, and convolve both the DIRBE/IRAS data and the noise with a one-degree Gaussian. As a consequence, our results are insensitive to the zero point of the 100$\mu$m maps. Using this procedure, we find no statistically significant correlation between the 145 GHz B03 and 100$\mu$m data in either the B03 deep ($b \lesssim -30$) or shallow ($b \lesssim -20$) fields from which the CMB power spectrum is derived.

The same analysis applied to the 245 GHz and 345 GHz B03 data results in very clear correlations with the 100 $\mu$m SFD map. The amplitude of these correlations, described in more detail in Masi et al. (2005), provides an empirical scaling of the observed surface brightness of the 100 $\mu$m dust to 145 GHz. When applied to the SFD map, this empirical scaling implies *r.m.s* fluctuations due to unpolarized dust of about 1 $\mu$K in the B03 deep region at the angular scales of interest. This is roughly two orders of magnitude below the CMB contribution, and will result in a correspondingly negligible impact on the estimate of the CMB power spectrum.

### 3.7. *Features in the Temperature Power Spectrum*

A series of acoustic peaks is readily apparent in the B03 power spectrum. As has become common practice (see, for example, de Bernardis et al. (2002); Ruhl et al. (2003); Page et al. (2003)), we calculate a model independent characterization of the location, amplitude, and significance of the features in the power spectrum through a comparison of the goodness of fit of a parabola (or Gaussian) to each set of five contiguous bins[3]. In this work, we fit a Gaussian to the band powers in the vicinity of the first peak, and a parabola to the other features.

[3] While the result is relatively insensitive to the number of bins that are fit, as the subsets get larger than the characteristic size of the features in the spectrum, the reduced $\chi^2$ clearly will degrade. Five bins is found to be the largest set that does not result in a poor goodness of fit statistic over the full range in $\ell$.

As is well known, the likelihoods of the band powers are not Gaussian distributed [Bond et al. (1998, 2000)]. We therefore transform to the "offset log-normal" variables whose likelihood distributions are better approximated by a Gaussian [Bartlett et al. (2000); Bond et al. (2000)]. The transformation is a simple one,

$$Z_b \equiv \ln(\mathcal{C}_b + x_b)$$

where the noise offsets, $x_b$, are determined from the (binned and deconvolved) $\widetilde{N}_\ell$ as derived from the noise Monte Carlos. The inverse Fisher (covariance) matrix must similarly be transformed,

$$(F^Z)^{-1}_{bb'} = \frac{F^{-1}_{bb'}}{(\mathcal{C}_b + x_b)(\mathcal{C}_{b'} + x_{b'})}.$$

In addition, the models to be fit are binned into bandpowers according to the same instrumental window functions, $W_\ell$, (shown in Figure 6) which are applied to the raw spectra

$$\mathcal{C}^{\rm xx}_b \equiv \frac{\mathcal{I}\left[W^b_\ell \mathcal{C}^{\rm xx}_\ell\right]}{\mathcal{I}\left[W^b_\ell\right]},$$

where the logarithmic binning operator is defined as

$$\mathcal{I}\left[f_\ell\right] \equiv \sum_\ell \frac{(\ell + \frac{1}{2})}{\ell(\ell+1)} f_\ell.$$

The parabolic model,

$$\mathcal{C}^m_\ell = \mathcal{C}_c(\ell - \ell_0)^2 + \mathcal{C}_0$$

is similarly transformed using the offset log-normal approximation, and the three dimensional likelihoods are calculated directly on a grid about each of the best fit locations. The $\Delta\chi^2$ contours for the curvature-marginalized likelihoods are shown in Figure 6.

In previously published B98 data, the significance of a detection has been determined by the curvature of the likelihood at the peak of the distribution [de Bernardis et al. (2002); Ruhl et al. (2003)]. However, as is evident in Figure 7, the distributions are highly non-Gaussian. We therefore determine the significance of the detections from the amplitude of the marginalized likelihood at zero curvature.

The first three peaks and three dips in the power spectrum are detected with high confidence. Although the data favor a fourth peak in the vicinity of $\ell = 1055$, with an amplitude of $\mathcal{C}_{1055} = 1020\ \mu K^2$, the marginalized likelihood for the curvature parameter is not inconsistent with zero. For comparison, the same analysis was applied to the B98 data from the Ruhl et al. (2003) release, as well as the binned first-year WMAP data [Bennett et al. (2003a)]. The results of all three analyses are compared in Table 3, and indicate a remarkable degree of consistency between the three independent experiments.

The degree of concordance in temperature observations is further illustrated in Figure 5, which shows a compilation of the power spectrum estimates derived from four experiments, representing four very different experimental approaches, with observations probing nearly a decade in electromagnetic frequency.

## 4. CONCLUSION

We derive an estimate of the angular power spectrum of the CMB from the data obtained with the 145 GHz polarization sensitive bolometers that flew on the January

2003 flight of BOOMERANG. The 245 and 345 GHz channels place stringent limits on the level of foreground contamination. We characterize the systematic effects that result from various instrumental calibration uncertainties with Monte Carlo analyses, and verify the consistency of the data with jackknife tests.

The B03 data are the first to be obtained using PSBs, which are identical in design to the polarized pixels in the *Planck* HFI focal plane. The sensitivity per resolution element achieved in the B03 deep field is comparable to that anticipated by *Planck* at 143 GHz. The high signal to noise of the temperature data results in a sample variance limited estimate of the power spectrum at multipoles $\ell \lesssim 900$.

The B03 data presented in this work represent the most precise measurements to date of the angular power spectrum between $600 \lesssim \ell \lesssim 1200$. In this regard, B03 plays a valuable role in bridging the gap between the all-sky WMAP survey at $\ell \lesssim 600$, and the high angular resolution data from terrestrial observations above $\ell \gtrsim 1200$. We characterize a series of features in the power spectrum which extend to multipoles $\ell \gtrsim 1000$, consistent with those expected from acoustic oscillations in the primordial plasma in the context of standard cosmologies.

## ACKNOWLEDGEMENTS

We gratefully acknowledge support from the CIAR, CSA, and NSERC in Canada, ASI, University La Sapienza and PNRA in Italy, PPARC and the Leverhulme Trust in the UK, and NASA (awards NAG5-9251 and NAG5-12723) and NSF (awards OPP-9980654 and OPP-0407592) in the USA. Additional support for detector development was provided by CIT and JPL. CBN acknowledges support from a Sloan Foundation Fellowship, WCJ and TEM were partially supported by NASA GSRP Fellowships. Field, logistical, and flight support were supplied by USAP and NSBF; data recovery was particularly appreciated. This research used resources at NERSC, supported by the DOE under Contract No. DE-AC03-76SF00098, and the MacKenzie cluster at CITA, funded by the Canada Foundation for Innovation. We also thank the CASPUR (Rome-ITALY) computational facilities and the Applied Cluster Computing Technologies Group at the Jet Propulsion Laboratory for computing time and technical support. Some of the results in this paper have been derived using the HEALPix package [Górski et al. (2005)], and nearly all have benefitted from the FFTW implementation of discrete Fourier transforms [Frigo & Johnson (2005)].

TABLE 3
FEATURES IN THE TEMPERATURE POWER SPECTRUM

| feature | $\ell_{\rm B03}$ | $\Delta T^2_{\rm B03}$ | $\ell_{\rm B98}$ | $\Delta T^2_{\rm B98}$ | $\ell_{\rm WMAP}$ | $\Delta T^2_{\rm WMAP}$ |
|---|---|---|---|---|---|---|
| Peak 1 | $214\ ^{+9}_{-12}$ | $5614\ ^{+450}_{-443}$ | $217\ ^{+10}_{-10}$ | $5551\ ^{+477}_{-443}$ | $222\ ^{+3}_{-2}$ | $5385\ ^{+147}_{-157}$ |
| Valley 1 | $413\ ^{+10}_{-5}$ | $1717\ ^{+133}_{-70}$ | $411\ ^{+9}_{-7}$ | $1870\ ^{+136}_{-120}$ | $418\ ^{+5}_{-4}$ | $1660\ ^{+62}_{-62}$ |
| Peak 2 | $529\ ^{+14}_{-6}$ | $2419\ ^{+125}_{-128}$ | $526\ ^{+17}_{-14}$ | $2316\ ^{+119}_{-121}$ | $530\ ^{+15}_{-8}$ | $2404\ ^{+89}_{-64}$ |
| Valley 2 | $659\ ^{+12}_{-11}$ | $1780\ ^{+131}_{-165}$ | $(677)\ ^{+65}_{-29}$ | $(1958)\ ^{+200}_{-170}$ | — | — |
| Peak 3 | $781\ ^{+15}_{-22}$ | $2166\ ^{+208}_{-216}$ | $(766)\ ^{+42}_{-43}$ | $(2080)\ ^{+261}_{-227}$ | — | — |
| Valley 3 | $1015\ ^{+26}_{-23}$ | $991\ ^{+137}_{-192}$ | — | — | — | — |
| Peak 4 | $(1055)\ ^{+58}_{-56}$ | $(1024)\ ^{+254}_{-271}$ | — | — | — | — |

A comparison of the locations and amplitudes of the features in the temperature power spectrum derived from the B03, B98, and WMAP datasets. The values and ($1\sigma$) errors are obtained from the marginalized likelihood distributions directly. Values in parenthesis indicate a curvature parameter consistent with zero at $2\sigma$ level, or greater (that is, a marginalized likelihood for the curvature parameter for which $\mathcal{L}(\mathcal{C}_c = 0) \geq 2\sigma$). Note that this analysis has been performed on the binned WMAP data for better comparison with the BOOMERANG window functions. The full resolution WMAP spectrum provides constraints on the first peak and dip locations that are stronger than (but also consistent with) those reported here. For the full resolution analysis of the first year WMAP data, see Page et al. (2003).

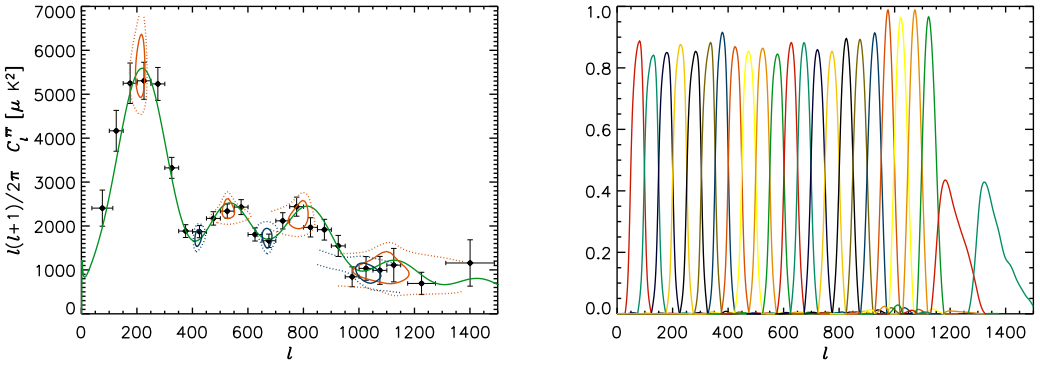


FIG. 6.— The left panel shows the CMB spectrum with the one and two-sigma $\Delta\chi^2$ contours for the fits shown in red (blue) for the features determined to have negative (positive) curvature. The likelihoods have been marginalized over the curvature parameter. The fourth "peak" only marginally favors negative curvature over a flat bandpower, and is not considered a detection. The right panel shows the window functions used in the generation of the band power estimates.

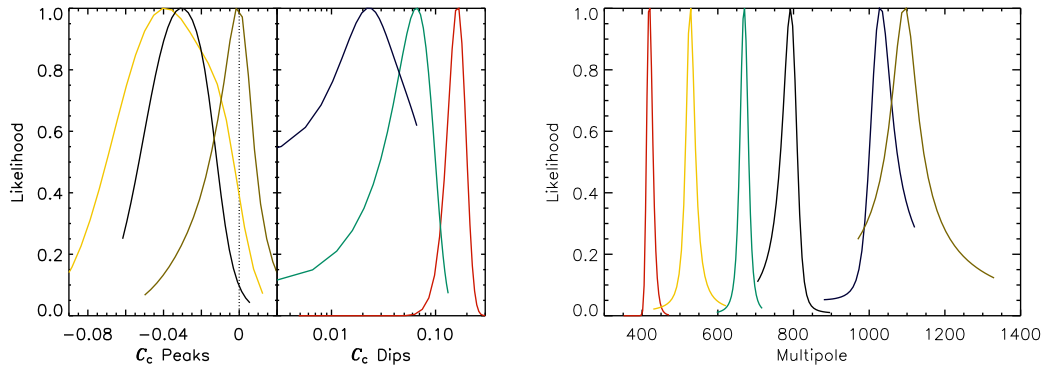


FIG. 7.— The marginalized likelihoods for the curvature parameter, $\mathcal{C}_c$, (at left) and the multipole, $\ell_0$, (at right) of each feature in the temperature power spectrum. All three dips in the power spectrum are detected with high confidence, whereas only the first three peaks are detected with curvature significantly different than zero. The data around the first peak are fit with a Gaussian rather than a parabolic model, and the likelihood contours for this feature are not shown.

REFERENCES

Bartlett, J. G., Douspis, M., Blanchard, A., & Le Dour, M. 2000, A&AS, 146, 507, astro-ph/9903045
Bennett, C. L. et al. 2003a, Astrophysical Journal Supplement Series, 148, 1
—. 2003b, Astrophysical Journal, 583, 1
Benoît, A. et al. 2003, Astronomy and Astrophysics, 399, L19
Bond, J. R., Jaffe, A. H., & Knox, L. 1998, Physical Review D, 57, 2117
—. 2000, Astrophys. J. , 533, 19
Borrill, J. 1999, in AIP Conf. Proc. 476: 3K cosmology, 277
Brandt, W. N., Lawrence, C. R., Readhead, A. C. S., Pakianathan, J. N., & Fiola, T. M. 1994, Astrophysical Journal, 424, 1
Bridle, S. L., Crittenden, R., Melchiorri, A., Hobson, M. P., Kneissl, R., & Lasenby, A. N. 2002, Mon. Not. Roy. Astron. Soc. , 335, 1193
Contaldi, C. R. et al. 2005, in preparation
Crill, B. P. et al. 2003, Astrophys. J. Suppl. , 148, 527
de Bernardis, P. et al. 2000, Nature, 404, 955
—. 2002, Astrophysical Journal, 564, 559
de Gasperis, G., Balbi, A., Cabella, P., Natoli, P., & Vittorio, N. 2005, Astr. & Astroph. , 436, 1159
de Oliveira-Costa, A. 2004, in Astronomical Polarimetry - Current Status and Future Directions, astro-ph/0406358
de Oliveira-Costa, A., Tegmark, M., Gutierrez, C. M., Jones, A. W., Davies, R. D., Lasenby, A. N., Rebolo, R., & Watson, R. A. 1999, Astrophys. J. Lett. , 527, L9
Dickinson, C. et al. 2004, Mon. Not. Roy. Astron. Soc. , 353, 732
Finkbeiner, D., Davis, M., & Schlegel, D. 1999, Astrophysical Journal, 524, 2
Frigo, M. & Johnson, S. G. 2005, Proceedings of the IEEE, 93, 216
Górski, K. M., Hivon, E., Banday, A. J., Wandelt, B. D., Hansen, F. K., Reinecke, M., & Bartelmann, M. 2005, Astrophys. J. , 622, 759
Halverson, N. W. et al. 2002, Astrophysical Journal, 568, 38
Hauser, M. G., Kelsall, T., Leisawitz, D., & Weiland, J. 1998, COBE Ref. Pub. No. 98-A
Hinshaw, G. et al. 2003, Astrophysical Journal Supplement Series, 148, 135
Hivon, E., Górski, K. M., Netterfield, C. B., Crill, B. P., Prunet, S., & Hansen, F. 2002, Astrophysical Journal, 567, 2
Jones, W. C. 2005, PhD thesis, California Institute of Technology
Jones, W. C., Bhatia, R. S., Bock, J. J., & Lange, A. E. 2003, Proc. SPIE Int. Soc. Opt. Eng., 4855
Jones, W. C., Montroy, T., Contaldi, C. R., Lange, A. E., Netterfield, C. B., & Ruhl, J. E. 2005, *in preparation*
Kuo, C. L. et al. 2004, Astrophys. J. , 600, 32
Lee, A. T. et al. 2001, Astrophysical Journal Letters, 561, L1
MacTavish, C. et al. 2005, *...submitted to Astrophys. J.*
Masi, S. et al. 2001, Astrophys. J. Lett. , 553, L93, astro-ph/0101539
—. 2005, *...submitted to Astr. & Astroph.*
Montroy, T. et al. 2003, New Astronomy Review, 47, 1057
—. 2005, *...submitted to Astrophys. J.*
Montroy, T. E. 2002, PhD thesis, University of California, Santa Barbara
Netterfield, C. B. et al. 2002, Astrophysical Journal, 571, 604
Neugebauer, G. et al. 1984, Astrophys. J. Lett. , 278, L1
Page, L. et al. 2003, Astrophysical Journal Supplement Series, 148, 233
Piacentini, F. et al. 2005, *...submitted to Astrophys. J.*
Polenta, G., Marnucci, D., Balbi, A., de Bernardis, P., Hivon, E., Masi, S., Natoli, P., & Vittorio, N. 2004, astro-ph/0402428
Prunet, S. et al. 2001, in Mining the Sky, 421
Readhead, A. C. S. et al. 2004, Astrophysical Journal, 609, 498
Ruhl, J. E. et al. 2003, Astrophys. J. , 599, 786, astro-ph/0212229
Schlegel, D. J., Finkbeiner, D. P., & Davis, M. 1998, Astrophys. J. , 500, 525
Tristram, M., Macías-Pérez, J. F., Renault, C., & Santos, D. 2005, Monthly Notices of the Royal Astronomical Society, 358, 833